SMA Memo #154

Total Power Atmospheric Phase Correction at the SMA

James Battat

First released on December 07, 2004
Last revised on December 07, 2004

ABSTRACT

Fluctuations in atmospheric water vapor content along the line of sight of an antenna alter the phase of the incoming astronomical signal. At submillimeter wavelengths these phase errors limit the angular resolution and reduce the correlated flux in an interferometer. We have developed and installed a total power phase correction system at the Submillimeter Array (SMA) on Mauna Kea to monitor and correct for atmospheric phase errors. Using our system in January, 2004, we monitored fluctuations in the difference of the total power between antennas to reliably track atmospheric phase fluctuations. For example, in a 20 minute data set with a 2.5 second integration time we reduced the rms phase error from 72° to 27°, corresponding to a residual differential path of 90 μm between antennas. This improved the coherence from 0.45 to 0.90. We believe that our system provides the most sensitive continuum measurement to date of the differential water column between two antennas.

Because this total power phase correction scheme is highly sensitive to receiver gain fluctuations, we developed a gain stabilization servo system to improve the SMA heterodyne receiver stability from a part in a few hundred (rms to mean) to 1 part in 6,000 at 230 GHz. This order of magnitude improvement over the intrinsic stability of most of the SMA receiving systems sets the instrumental noise floor for total power phase correction at $\sim 10°$ in median 230 GHz observing conditions at the SMA.

In this memo, we provide background describing the causes and effects of atmospheric phase fluctuations in submillimeter wave interferometry. In addition, we describe the total power phase correction technique. We also discuss some instrumental gain stability requirements and present the system we designed to reach these goals. Finally, we present results of the 2004 January phase correction experiment at the SMA and discuss future prospects for phase correction at the SMA.

1. A Description of the Problem

The Submillimeter Array[1] (SMA) is the world's first interferometer devoted to the study of frequencies in the range of 180-900 GHz. With baselines up to 500 meters, its diffraction limited resolution is 0.1-0.″5. Atmospheric phase fluctuations, however, typically limit the angular resolution to $\sim 1''$ when phase correction techniques such as self-calibration are not possible. Furthermore, the atmospheric phase errors reduce the recoverable flux (coherence) in an observation and limit the available observing time, especially at the highest frequencies. Atmospheric phase correction, using total power radiometry, can improve the angular resolution and the coherence of observations. In addition, it can enable observations that, in the absence of phase correction, would have been impossible due to unstable atmospheric conditions.

In an attempt to minimize the atmospheric effects, great care has been taken to situate submillimeter wavelength interferometers at sites of both good atmospheric transmission and stability (Paine et al. 2000; Peterson et al. 2003; Matsushita & Matsuo 2003). These site investigations have revealed that Mauna Kea in Hawaii, the Atacama Desert in northern Chile and the South Pole are favorable for submillimeter wave astronomy. However, even at these sites the resolution of submillimeter wave interferometers is limited by atmospheric phase fluctuations. In order for the SMA and future submillimeter wave interferometers (notably ALMA, the Atacama Large Millimeter Array) to reliably image with sub-arcsecond resolution, it is imperative to develop robust atmospheric phase correction systems.

At centimeter wavelengths, atmospheric phase errors can be tracked by monitoring strong, nearby, compact calibration objects such as quasars. At submillimeter wavelengths where atmospheric phase errors are more pronounced, one finds fewer suitable phase calibration sources[2]. Self-calibration requires a sufficient on source signal-to-noise ratio in an integration time over which the atmospheric fluctuations are not prohibitively large. At the SMA, with a 30 second integration time at 345 GHz and assuming a 10 m s^{-1} wind speed, the residual phase error is 1 radian. Furthermore, the SNR will be as low as $\sim$2 for a source flux of 0.2 Jy. At higher frequencies, the prospects worsen (residual phase errors grow linearly with frequency). Furthermore, significant atmospheric fluctuations occur on short timescales (often down to 1 second), defined by the antenna separation divided by the wind speed along the baseline, and therefore a more robust phase calibration scheme is needed to account for these rapid fluctuations.

In this memo we describe a submillimeter wavelength atmospheric continuum emission detection system, developed for the SMA, to correct for atmospheric phase fluctuations. In January, 2004, we installed and observed with the system on two of the SMA telescopes and in this memo we present results from those observations. We begin by describing the origin and nature of the

[1]The Submillimeter Array is a joint project between the Smithsonian Astrophysical Observatory and the Academia Sinica Institute of Astronomy and Astrophysics, and is funded by the Smithsonian Institution and the Academia Sinica. For more on the SMA and its characteristics, see Ho et al. (2004).

[2]Butler (2003) points out that this may not be the case. But there is uncertainty as to the angular size of the emitting regions of the early type galaxies that he includes in his analysis. If the sources are spatially resolved by the interferometer then they would be poor choices for phase calibrators. If the emission is due to dust, then one could expect angular sizes of $1''$. If, however, the emission is due to a central AGN or other compact regions, then the emitting regions could be sufficiently small.

atmospheric phase fluctuations. Next we describe the total power atmospheric phase correction scheme. We then describe our receiver gain stabilization system, developed in response to the need for highly stable continuum measurements of atmospheric emission. Finally, we present results of our atmospheric phase correction observations and discuss the future prospects for atmospheric phase correction at the SMA.

1.1. Atmospheric effects

An interferometer derives information about source position and structure from the relative phase of the measured electromagnetic waves. The atmosphere changes the phase of a propagating wave and therefore introduces noise into the astronomical measurement. Here we describe the origin and effects of the atmospheric phase errors.

There are both ionized and neutral media in the atmosphere through which an elecromagnetic wave originating at an astronomical source must travel before reaching a ground-based telescope. The index of refraction, n, of the atmosphere is greater than unity, and thus the wave will be retarded with respect to free space propagation because of its decreased phase velocity, c/n. The product of this time delay, Δt, and the speed of light in a vacuum, c, defines an excess electrical path, L where

$$L \equiv c\Delta t = \int [n(y) - 1]\, dy \tag{1}$$

Here y is the direction of propagation of the electromagnetic wave. Because the index of refraction depends only weakly on frequency at submillimeter wavelengths away from resonant frequencies (i.e. it is non-dispersive, see Figure 1), the phase of the astronomical signal, ϕ, is related to wavelength in the following way

$$\phi = 360^\circ \frac{L}{\lambda} \tag{2}$$

where ϕ is in degrees and the units of L and λ are the same.

At 20 GHz, the excess electrical path due to the ionosphere is 1% of that due to the troposphere (Thompson et al. 2001, page 555). Because the magnitude of the ionospheric effect scales as λ^2, the ionospheric path is negligible at submillimeter wavelengths and we only need to consider the tropospheric effects on phase delay. Furthermore, an interferometer is only sensitive to the differential path, $\Delta L \equiv L_2 - L_1$, between the lines of sight of antenna pairs (see Figure 2). Thus the phase error, $\Delta\phi$, introduced by the atmosphere is written

$$\Delta\phi = 360^\circ \frac{\Delta L}{\lambda} \approx 30^\circ \left(\frac{\nu}{230\ \mathrm{GHz}}\right)\left(\frac{\Delta L}{100\ \mu\mathrm{m}}\right) \tag{3}$$

where $\Delta\phi$ has units of degrees and the second form is a convenient expression to remember in submillimeter wave astronomy.

The dry troposphere introduces about 2.3 meters of excess electrical path, while the water vapor adds approximately 0.04 meters more for a site at an altitude of 4 km (Thompson et al. 2001). Thus the dry delay is approximatly 8 ns and the wet delay is 0.15 ns. If the troposphere were perfectly homogeneous, then L would be constant along all lines of sight at a given angle of elevation, so $\Delta L = 0$ and there would be no atmospheric phase error. Although some components of the troposphere are either homogeneously distributed (e.g. oxygen, nitrogen) or slowly time

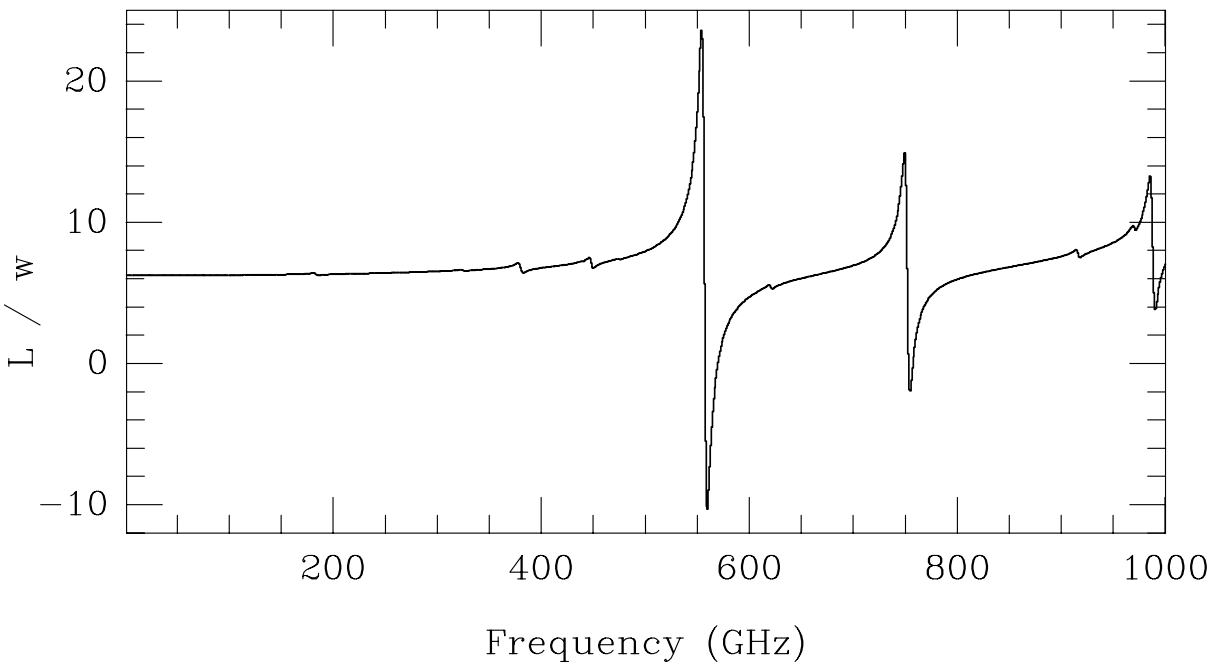

Fig. 1.— The electrical path as a function of water vapor column. Below 400 GHz the water vapor is highly non-dispersive, even at resonance frequencies (e.g. 22, 183 GHz). Above 400 GHz, the non-dispersive approximation begins to weaken. Plot taken from (Sutton & Hueckstaedt 1996), in which they describe the precipitable water vapor with the symbol w, in this memo we use pwv. See also Paine, S. (2004) for freely available code to make your own plots of L/w vs. ν.

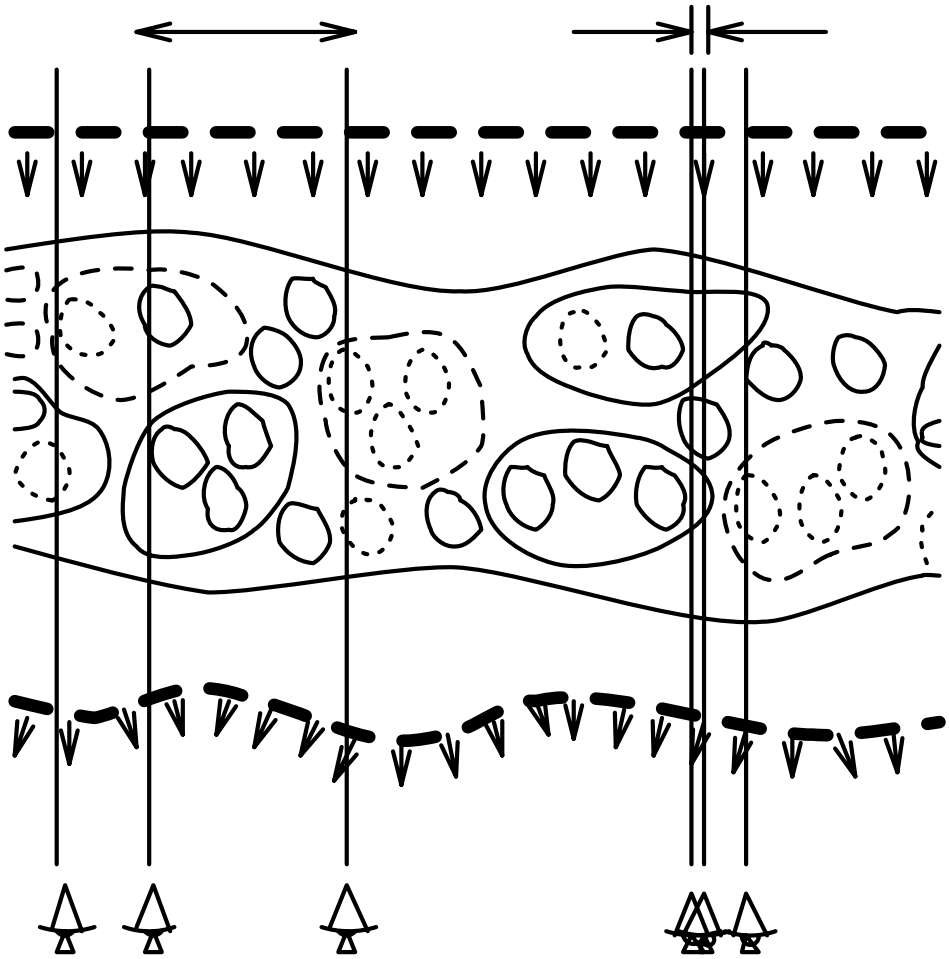

Fig. 2.— Phase errors are caused by a non-homogeneous water vapor distribution. This is shown schematically by cells of water vapor over-density (solid lines) and under-density (dashed lines) with respect to the mean density. A plane wave incident on the water vapor distribution emerges with a distorted wave front. Furthermore, this diagram nicely shows that the phase error only depends on water vapor structures that are smaller than the baseline lengths. Cells that cover both lines of sight of an antenna pair will introduce an overall phase delay, but no differential delay on that baseline. Also, one can see how the phase errors grow with baseline because there are an increasing number of cells whose size is smaller than the baseline. Taken from (Carilli & Holdaway 1999, after Desai, K. (1993)).

variable (e.g. ozone), the water content is poorly mixed and rapidly fluctuating. Water vapor is the dominant source of atmospheric phase errors in submillimeter wave interferometry.

As shown in Figure 1, the electrical path introduced by water vapor is ~ 6.5 times the water vapor column, (also called precipitable water vapor, *pwv*). Typically, at good submillimeter wavelength astronomy sites, the zenith *pwv* ranges from 0.25-5 mm. The phase shift and attenuation that result from the presence of water vapor are related by the Kramers-Kronig relationship. The optical depth, τ is linearly related to the *pwv* content. At 225 GHz on Mauna Kea, Masson (1994) shows that

$$\tau_{225} = 0.01 + 0.04\ pwv \tag{4}$$

where the 0.01 offset characterizes the atmospheric attenuation of a dry atmosphere, and is predominantly due to oxygen. In this equation, *pwv* has units of millimeters.

Despite the relationship between signal phase and signal attenuation along a single line of sight, there is little correlation between the mean opacity and the phase stability (see Figure 3). In other words, an atmosphere with significant but unchanging water vapor content would be highly opaque, yet no temporal fluctuations in differential phase would be seen between antenna pairs. In practice a distribution of water vapor cells is blown across the array, creating fluctuations in differential phase between antennas. These cells exist in a wide range of sizes (typically from under a meter up to many kilometers), and the magnitude of the differential phase depends on the separation (baseline) between antenna pairs. The root phase structure function is a quantity that describes the distribution of phase error with baseline length and is defined as

$$\sigma_{\Delta\phi}(b) = \sqrt{D_\phi(b)} \equiv \sqrt{\left\langle \left[\phi\left(x+b\right) - \phi\left(x\right)\right]^2 \right\rangle} \tag{5}$$

where $\phi(x)$ is the phase along the line of sight at position x and $\sigma_{\Delta\phi}$ is the expected rms phase error between antennas separated by b. In practice, the ensemble average, $\langle \ldots \rangle$, is replaced by a temporal average.

In the well established Kolmogorov description of atmospheric turbulence, the root phase structure function, which describes how phase errors depend on the antenna separation (a.k.a. the baseline, b), is a twice broken power law proportional to $b^{\beta/2}$, where $\beta/2$ is called the Kolmogorov exponent. For baselines shorter than the vertical extent, W, of the turbulent layer ($b \lesssim 0.5 - 2$ km), the turbulence is approximately isotropic in three dimensions and $\beta/2 = 5/6$. For baselines larger than W but smaller than the coherence length of water vapor cells, L_0, a two dimensional approximation to the turbulence yields $\beta/2 = 1/3$ (Carilli & Holdaway 1999). Finally, on size scales larger than L_0 (typically 5-10 km), the phase errors do not increase with baseline ($\beta/2 = 0$). Because of this outer scale and the associated long timescales, Very Long Baseline Interferometry ($b > 1000$ km) is viable. Figure 4 shows that data taken with the Very Large Array (VLA) strongly supports the three-regime power law description of the root phase structure function and the Kolmogorov exponents determined from a best fit to the data are similar to the theoretical predictions. In addition, they find that $W \sim 1.2$ km. Although the value of W will depend on site location and weather conditions, W is typically 0.5-2 km (Woody et al. 2000; Robson et al. 2001), and thus all SMA baselines fall in the 3D regime of Kolmogorov turbulence.

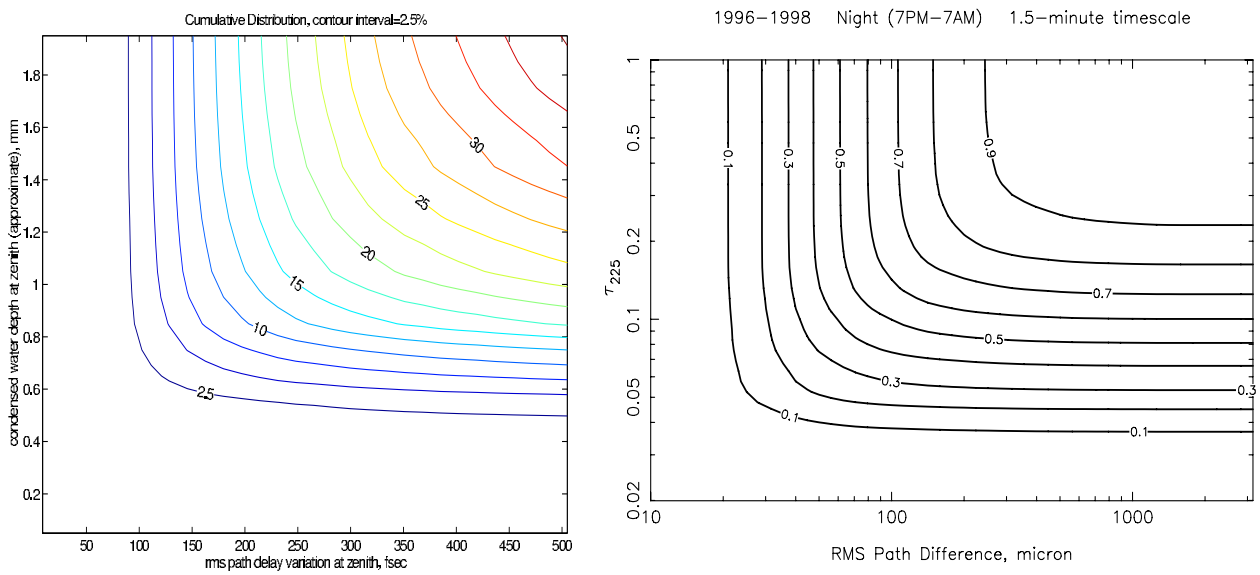

Fig. 3.—

Left: The cumulative joint distribution of path delay fluctuations on a 300 meter baseline (abscissa) and condensed water depth (ordinate). The contour labels are in percent. At each point, the plotted value is the fraction of time that conditions are equal to or better than the values on the axes. For example, at each point on the contour labeled "10" the conditions to the left and below that point occur 10% of all time. This data is derived from 6 years of site testing data at Chajnantor, the site in Chile where ALMA will be built. Plot and caption come from LAMA Memo #801 by L. D'Addario and M. Holdaway.

Right: A similar plot for data taken with the SAO Phase Monitor, a site testing interferometer on Mauna Kea that operated at 12 GHz on a 100 m baseline. In this plot, the ordinate is in units of 225 GHz opacity, which is related to *pwv* by Equation 4, and the abscissa is in units of differential excess path between the antenna pair. These contour labels are in fraction of total time. Plot provided by M. Gurwell. See Masson (1994) for more information about the SAO Phase Monitor.

The expected rms phase error between two antennas can be written as

$$\sigma_{\Delta\phi}(b) = K\left(\frac{\nu}{230\ \mathrm{GHz}}\right)\left(\frac{b}{100\ \mathrm{m}}\right)^{\beta/2}\csc^{\gamma}\theta_{EL} \tag{6}$$

where ν is the observing frequency, θ_{EL} is the elevation angle of the observation and γ is 1 or 1/2 for two or three dimensional turbulence, respectively. K is a constant that depends on atmospheric conditions, and has units of degrees (while K' will be in radians). Note that observations at the SMA will all be in the three dimensional turbulence regime where phase errors grow rapidly with baseline (typically $\beta/2 \approx 5/6$).

The *Taylor Hypothesis*, or *frozen screen approximation*, of atmospheric turbulence posits that if the turbulent intensity is low and the turbulence is largely stationary, then the cells of water vapor, to a good approximation, are blown bodily across the array, horizontally through the troposphere.[3] Under this assumption, it is possible to relate the spatial root phase structure function, $\sigma_{\Delta\phi}$, to a temporal phase structure function that describes the timescales over which the phase fluctuations occur by using the transformation, $b = v * (\mathrm{time})$, where v is the speed with which the water vapor cells are blown between antennas. The temporal phase structure function, $\Phi(f)$ is a broken power law with a corner frequency, $f_c \propto b/v$ and has the form

$$\Phi(f) \propto f^{-\alpha}. \tag{7}$$

Under the Taylor Hypothesis, it is possible to compute the root phase structure function from measurements of the temporal phase structure function on a single baseline. At frequencies higher than f_c, $\alpha_{high} = \beta/2 + 0.5$ and below f_c, $\alpha_{low} = \alpha_{high} - 1$. The SAO Phase Monitor on Mauna Kea (100 m baseline, 12 GHz observing frequency) measured the Kolmogorov exponents over many years in the 1990s (Masson 1994). Masson (1994) reported a median excess electrical path of ~ 100 μm and $\beta/2 = 0.75$. From the excess electrical path, we calculate $K \sim 30°$. In these conditions, the extrapolated zenith atmospheric phase error reaches 1 radian at 345 GHz on a 140 meter baseline. In addition, typical values of the time spectrum parameters are $f_c \sim 0.01$ Hz, and $\alpha_{high} = 1.25$ (Masson 1994).

From these measurements, it is possible to characterize the limiting atmospheric resolution achievable on Mauna Kea. This resolution, θ_{min}, is defined as

$$\theta_{min} = 0.7\frac{\lambda}{b_{max}}\ \mathrm{rad} \tag{8}$$

$$= 1.88\left(\frac{\nu}{230\ \mathrm{GHz}}\right)^{-1}\left(\frac{b_{max}}{100\ \mathrm{m}}\right)^{-1}\ \mathrm{arcsec} \tag{9}$$

where λ is the observing wavelength and b_{max} is an effective maximum baseline of the interferometer, defined here as the baseline at which the rms phase error reaches 1 radian. By rearranging Equation 6 and using K' defined as K in units of radians, we find that

$$b_{max}(\nu) = 100\left[\frac{1}{K'}\left(\frac{\nu}{230\ \mathrm{GHz}}\right)^{-1}\right]^{2/\beta}\ \mathrm{meters} \tag{10}$$

[3]Often, the tropospheric winds are faster and slightly shifted in direction with respect to the ground winds.

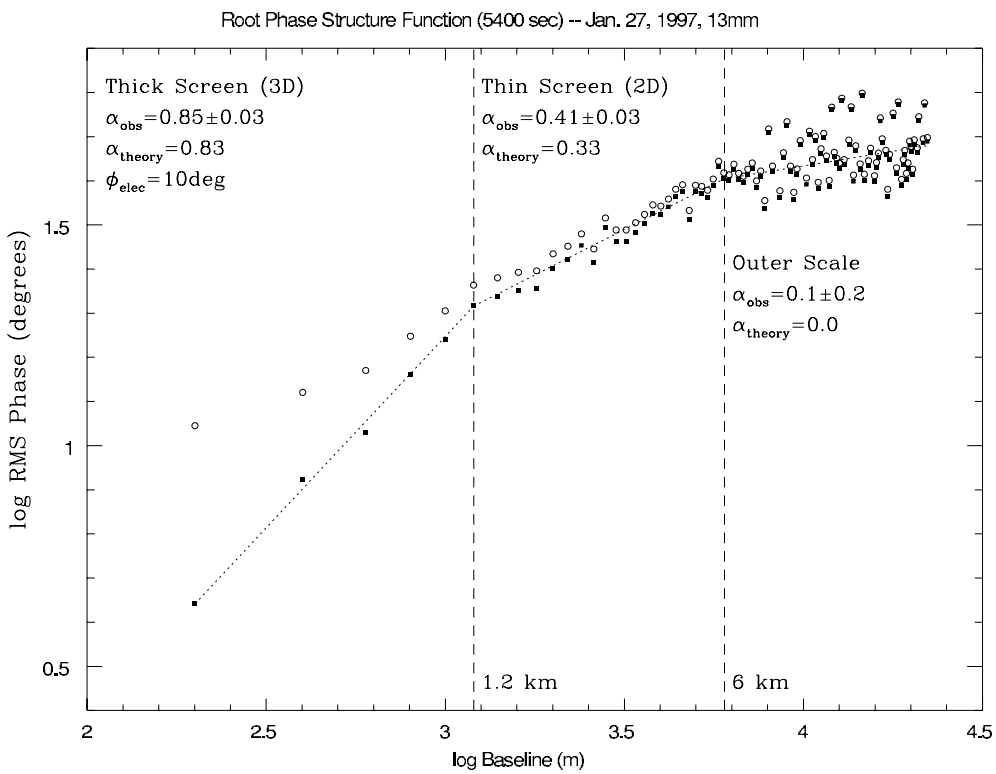

Fig. 4.— The root phase structure function as measured by the VLA. Here the Kolmogorov exponent (which I call $\beta/2$) is labeled α. The observations were taken in the BnA configuration at 22 GHz while monitoring a 1 Jy calibrator source over a period of 90 minutes. The open circles show the measured phase as a function of antenna separation, b. The filled squares show the same data with a constant instrumental phase error of 10° subtracted in quadrature. This plot is taken from Carilli & Holdaway (1999).

and thus the resolution, which has a weak dependence on frequency, can be written

$$\theta_{min} = 1.88 K'^{2/\beta} \left(\frac{\nu}{230 \text{ GHz}}\right)^{2/\beta - 1} \text{ arcsec.} \tag{11}$$

For the Mauna Kea median values $K = 30°$ and $\beta/2 = 0.75$ we find that

$$\theta_{min} = 0.79 \left(\frac{\nu}{230 \text{ GHz}}\right)^{1/3} \text{ arcsec.} \tag{12}$$

and we see that the limiting angular resolution degrades with increasing frequency. The median atmospheric resolution limits on Mauna Kea as a function of observing frequency are presented in Figure 5.

1.2. Atmospheric Effects on Visibility Data

For a phase error, $\Delta\phi$, the measured visibility, V_m, is related to the true visibility, V, by

$$V_m = V e^{i\Delta\phi}. \tag{13}$$

where $i = \sqrt{-1}$. Under the assumption that $\Delta\phi$ is a gaussian random variable, the coherence (the ratio of the expectation value of the measured visibility to the actual visibility) is

$$\frac{\langle V_m \rangle}{V} = e^{-\sigma^2_{\Delta\phi}/2} \tag{14}$$

where $\langle \ldots \rangle$ denotes an ensemble average and $\sigma_{\Delta\phi}$ is the rms phase error. The ensemble average is generally replaced by a temporal average (Thompson et al. 2001).

As we have shown above, the rms phase error is a function of baseline (Equation 6), and thus the coherence will depend on the baseline. In other words, the visibility data will be multiplied by a tapering window function, $W(b)$, that takes the form

$$W(b) = \exp\left\{-\frac{1}{2}\left[K'\left(\frac{\nu}{230 \text{ GHz}}\right)\left(\frac{b}{100 \text{ m}}\right)^{\beta/2}\right]^2\right\}. \tag{15}$$

where one must remember to use K', which is K expressed in radians. The atmospheric seeing function is given by the Fourier transformation of $W(b)$, and the interferometer resolution is the full width at half maximum (FWHM) of the seeing function. See Thompson et al. (2001) for a detailed description of atmospheric seeing disks and their dependence on $\beta/2$.

2. Total Power Phase Correction

Here we describe the total power phase correction technique. We begin with some theoretical constructs and then move to technical considerations such as the required receiver gain stability and optimal observing frequency.

Unlike traditional calibration techniques such as fast switching in which the phase between antennas is measured directly on a calibration source, in radiometric phase correction the observable is the receiver system noise temperature along the line of sight. If fluctuations in this quantity are

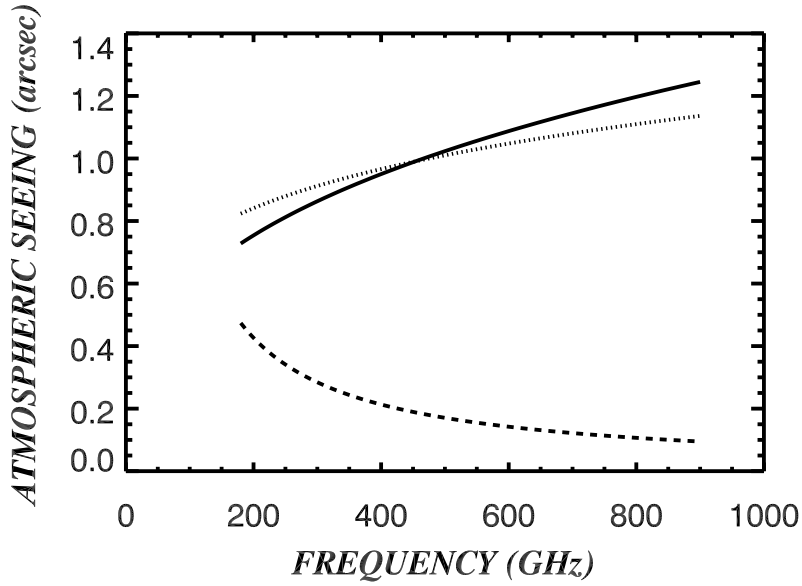

$\beta/2 = 0.75$		
ν	θ_{min}	b_{max}
GHz	arcsec	meters
230	0.79	238
345	0.91	138
400	0.95	113
690	1.14	55
850	1.22	41

Fig. 5.— The atmospheric limit to the angular resolution for median observing conditions as a function of frequency. The solid line shows the seeing for $\beta/2 = 3/4$ ($\theta_{min} \propto \nu^{1/3}$) as measured on Mauna Kea. The dotted line shows the Kolmogorov prediction for baselines smaller than the 2-D limit ($\beta/2 = 5/6$ and $\theta_{min} \propto \nu^{1/5}$). The effective maximum baseline, b_{max}, defined as the baseline at which the atmospheric phase errors reach 1 radian, is tabulated above for $\beta/2 = 3/4$. The dashed line at the bottom of the graph shows the diffraction limit of the SMA on the longest baseline (508 m).

dominated by fluctuations in the atmospheric brightness temperature, then it is feasible to monitor the atmospheric emission and infer the water vapor content along the line of sight. Differential water vapor content between antenna pairs is proportional to the atmospheric phase error on that baseline. This technique has great advantages over fast switching in that it measures the same water vapor that generates the phase errors during source observations. As a result, the derived phase correction is simultaneous and collinear with the source observation and, as a result, is independent of baseline length. One limitation to this technique is the instrumental noise floor due to the receiver stability.[4] The experimenter must carefully minimize this effect. Another restriction on the minimum residual phase error is the integration time. The phase fluctuations during an integration time will typically be equal to the uncorrected phase errors on a baseline of length $vt_{int}/2$, e.g. 5 meters for a 5 m s^{-1} wind and a 2.5 second integration time.

Radiometric phase correction makes use of the relationship between the real and imaginary parts of the index of refraction. In other words, water vapor will both retard and attenuate a propagating electromagnetic wave. As shown in Figure 6, water vapor is the dominant contributor to the atmospheric opacity (and therefore to the atmospheric brightness temperature) at submillimeter wavelengths. As the water vapor content changes, the atmospheric brightness temperature due to water vapor, $T_{bri}(wet)$ will also change (see Figure 7). These temperature changes will be accompanied by phase changes along the line of sight of an antenna, so that

$$\Delta\phi = k_\nu \Delta T_{bri}(wet) \tag{16}$$

where $\Delta T_{bri}(wet)$ is the differential temperature between two antennas caused by water vapor fluctuations and $\Delta\phi$ is defined in Equation 3. k_ν is a frequency dependent proportionality constant with units of degrees K^{-1}.

In Table 1, I have compiled the radiometric phase correction efforts of other groups. The mean residual differential electrical path during our total power phase correction experiment was 90 μm (25° at 230 GHz), though our system often corrected the differential path to 65 μm or less ($< 20°$ of phase at 230 GHz). During these tests, the receiver gain stability was approximately 1 part in 1,500 (as measured on an ambient temperature load). The noise floor can be improved with the gain stabilization system that we have developed, which should improve the quality of the phase correction.

There seems to be a general movement away from total power phase correction and toward water line monitoring (WLM). A cited reason for this shift is that WLM systems perform well even in the presence of liquid water and clouds in the atmosphere which are strong emitters but only weakly affect the signal phase. However little data exists with total power and water line monitoring systems performing side-by-side at submillimeter wavelengths, so this claim remains to be fully justified.[5]

It is worthwhile to mention some difficulties with total power phase correction at this point. First, one must ensure that the temperature scale is accurate and similar between antennas. If one does not have an accurate temperature scale at each antenna then more parameters are needed to

[4]Another limitation is the possible presence of liquid water in the atmosphere. This will be discussed later.

[5]IRAM has performed total power and WLM phase correction and has preliminary data relating the quality of the correction provided by each technique.

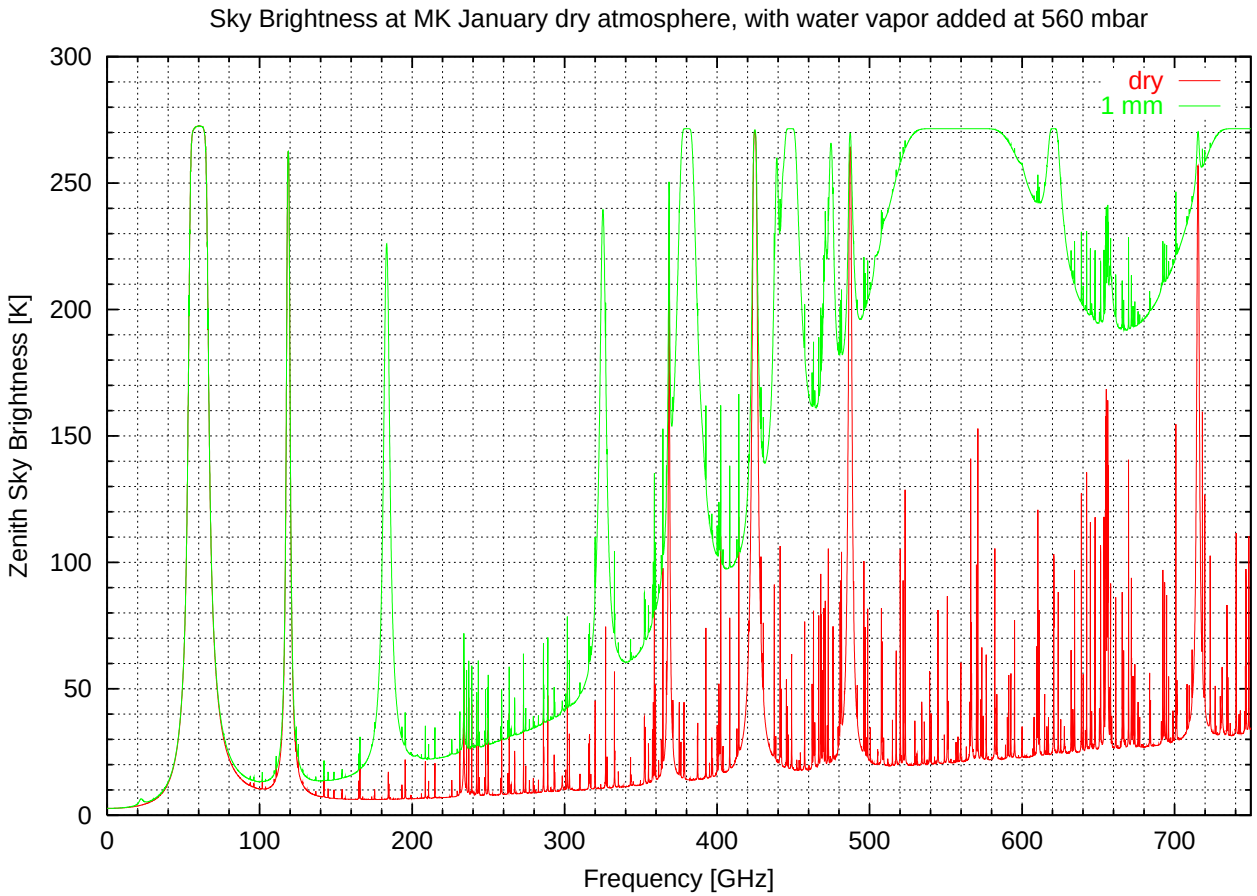

Fig. 6.— Atmospheric spectrum for a typical Mauna Kea atmospheric profile. A dry (0 mm *pwv*) brightness temperature profile is shown in red, while the effect of the addition of 1 mm *pwv* at 560 mbar is shown in green. Above 150 GHz and away from dry atmospheric emission lines, the brightness temperature in the atmospheric windows is dominated by the water vapor emission. This plot was made with the *am* Atmospheric Model program (Paine, S. 2004).

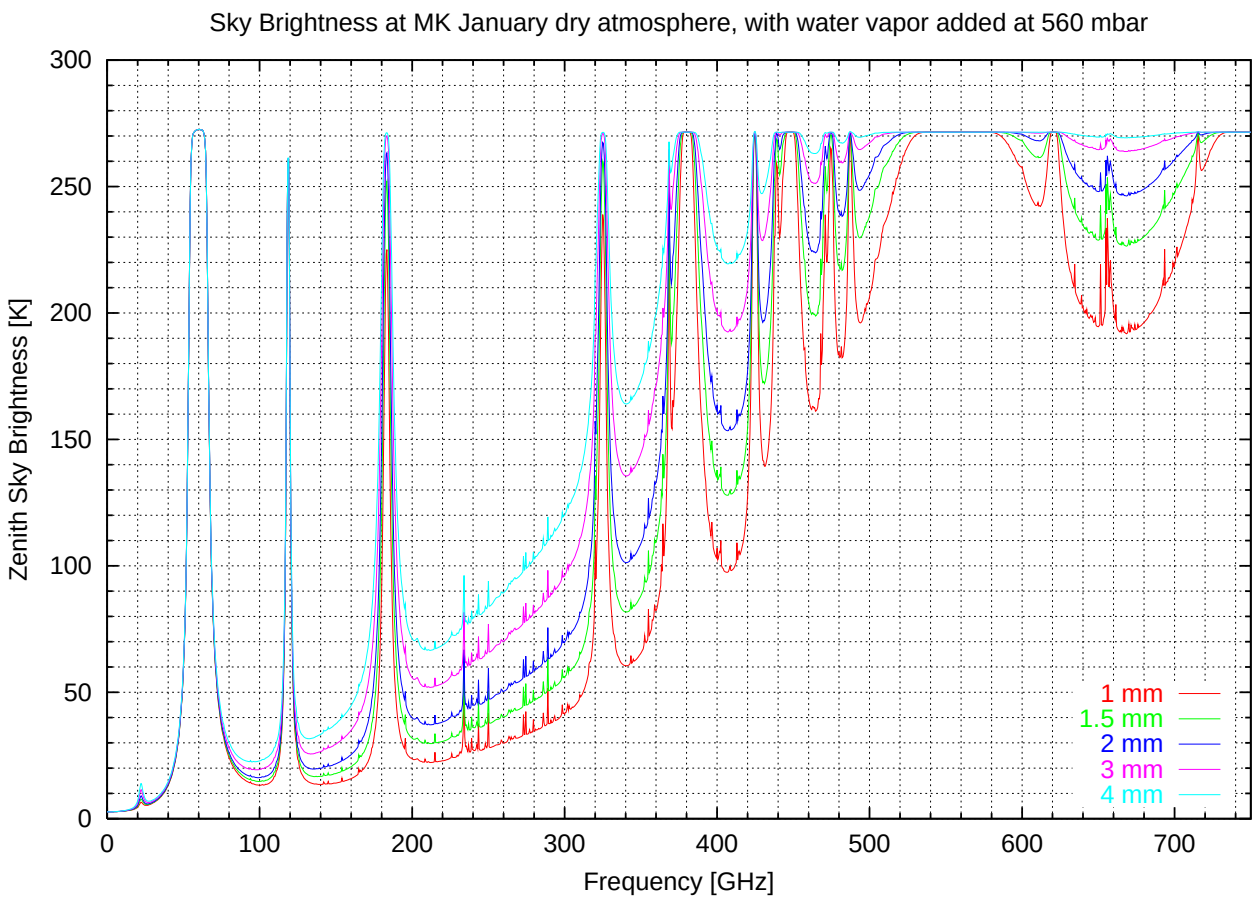

Fig. 7.— Atmospheric brightness temperature profiles for various values of *pwv*. This plot was generated by the *am* Atmospheric Model program (Paine, S. 2004).

describe the transformation from $\Delta T_{bri}(wet)$ to $\Delta\phi$. We treat this case later. Second, the value of k_ν can be determined from atmospheric models, but will depend on the unknown vertical profile of the water vapor, which is time-variable. It is possible to determine k_ν empirically by fitting $\Delta\phi$ to the actual phase error as measured by the interferometer while looking at a phase calibration source. In other words, one can empirically determine the scaling coefficient. Finally, any gain fluctuations in the receiving system will mimic atmospheric temperature fluctuations, and therefore introduce an error into the determination of $\Delta\phi$. The problem of receiver stability is a serious limit to all total power phase correction systems. In order to improve the stability of the SMA receivers, we designed a servo loop that stabilizes the receivers to 1 part in 6,000 (rms to mean). This system is described in detail in a separate paper (Battat 2005).

2.1. The Magnitude of Temperature Fluctuations

Given that the phase errors are related to the atmospheric brightness temperature fluctuations, one can ask what is the expected value of ΔT_{bri} (in K) per degree of phase error. In order to answer this question, we reformulate Equation 3 as

$$\Delta\phi = 112^\circ \left(\frac{\nu}{230\ \mathrm{GHz}}\right)\left(\frac{dL/dpwv}{6.5\ \mathrm{mm\ mm^{-1}}}\right)\left(\frac{dT_{bri}/dpwv}{16\ \mathrm{K\ mm^{-1}}}\right)^{-1}\Delta T_{bri} \tag{17}$$

where $dL/dpwv$ is a unitless quantity expressing the excess electrical path per unit water vapor column ($\sim$ 6.5 mm mm^{-1}, as shown in Figure 1), and $dT_{bri}/dpwv$ is called the "sensitivity" of the atmosphere which is a quantity that describes the change in atmospheric brightness temperature induced by a *pwv* fluctuation. This quantity will depend on both frequency and *pwv*. Figure 8 shows typical sensitivity profiles for a Mauna Kea atmosphere with various levels of mean water vapor content. For typical values of atmospheric sensitivity (16 K mm^{-1}) and $dL/dpwv$ (6.5 mm K^{-1}) at 230 GHz, $\Delta T_{bri}/\Delta\phi = 1/112$ K deg^{-1}. In median observing conditions ($pwv \sim 2$ mm) at the SMA, the sky brightness temperature is 45 K, and at 230 GHz the typical receiver temperature is 80 K (Tong 2004), thus the system temperature ($T_{sys} = T_{rx} + T_{bri}$) is 125 K and the signal to noise ratio per degree of phase change, defined as

$$\frac{SNR}{deg} = \frac{\Delta T_{bri}/\Delta\phi}{T_{sys}} \tag{18}$$

is 7 x 10^{-5}. The SNR/deg parameter depends on observing frequency and *pwv* content, but in all cases it is small (see Figure 9). Very stable receivers are therefore needed in order to ensure accurate detection of the sky brightness fluctuations.

2.2. Receiver Gain Stability Requirement

In the absence of source signal variations, fractional changes in the system temperature are due to both thermal noise and gain fluctuations which are independent and add in quadrature to give (Tiuri & Räisänen 1986)

$$\frac{\Delta T}{T_{sys}} = \sqrt{\left(\frac{1}{\sqrt{Bt_{int}}}\right)^2 + \left(\frac{\Delta G}{G}\right)^2} \tag{19}$$

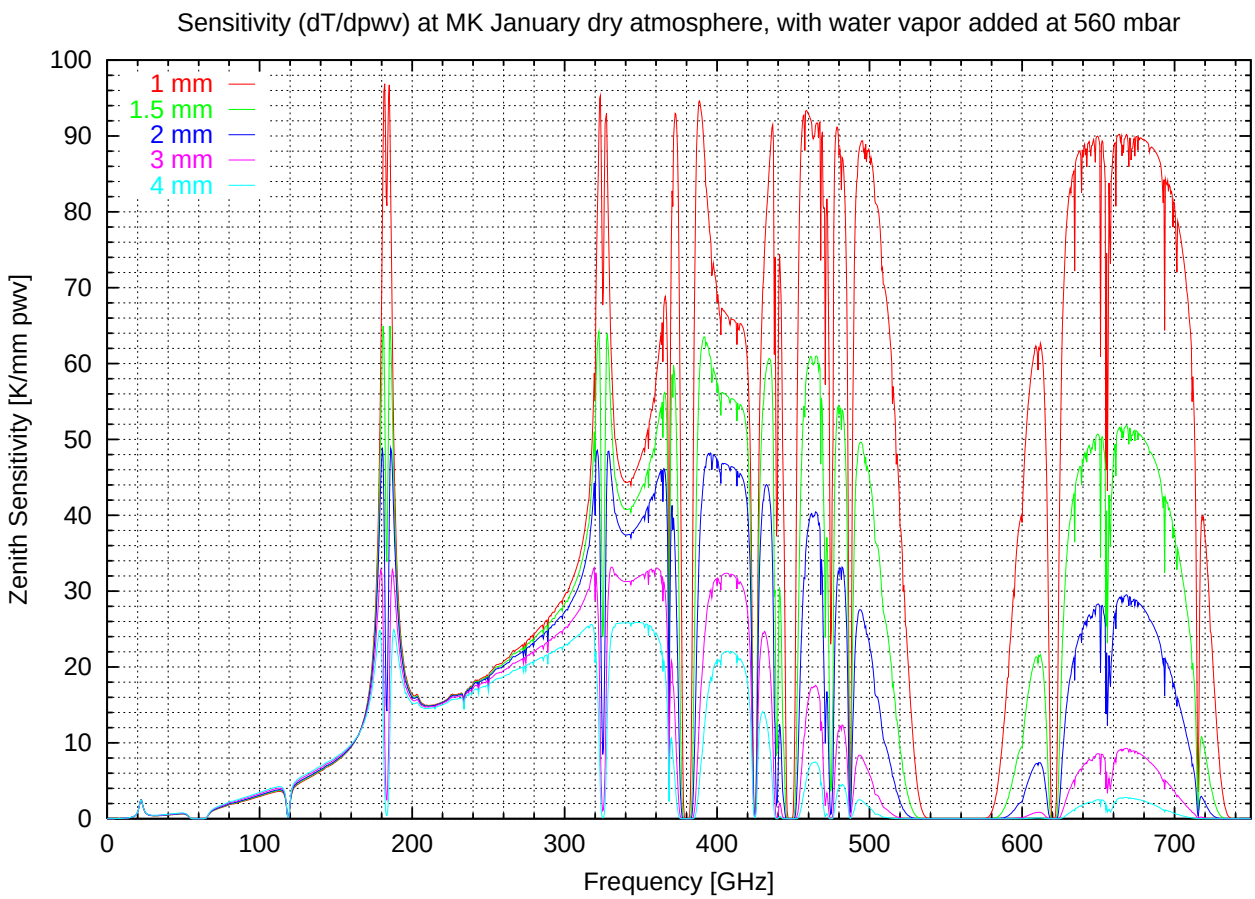

Fig. 8.— The atmospheric sensitivity, computed from the derivative of T_{bri} vs. ν at various mean levels of *pwv*. This plot was made using the *am* Atmospheric Model (Paine, S. 2004).

where B is the receiver bandwidth, t_{int} is the integration time and G is the gain of the receiving system. Typically, the thermal noise is much smaller than the effect of the gain fluctuations and thus Equation 19 simplifies to

$$\frac{\Delta T}{T_{sys}} \approx \frac{\Delta G}{G}. \tag{20}$$

For example, at the SMA, $B = 2.5$ GHz and the minimum $t_{int} \approx 2.5$ sec, thus $1/\sqrt{Bt_{int}} \lesssim 1$ x 10^{-5}. SMA receivers are typically stable to $\Delta G/G \sim 1/500$ and thus our approximation is valid, and we can replace ΔT_{bri} in Equation 17 with $T_{sys}\frac{\Delta G}{G}$ to determine the instrumental limit to phase correction performed with receivers of stability $\Delta G/G$

$$\Delta\phi \approx 20^\circ \left(\frac{\nu}{230\ \mathrm{GHz}}\right)\left(\frac{dL/dpwv}{6.5\ \mathrm{mm\ mm^{-1}}}\right)\left(\frac{dT_{bri}/dpwv}{16\ \mathrm{K\ mm^{-1}}}\right)^{-1}\left(\frac{T_{sys}}{125\ \mathrm{K}}\right)\left(\frac{\Delta G/G}{10^{-3}}\right) \tag{21}$$

where we have included an extra factor of $\sqrt{2}$ because the phase error depends on the quadrature sum of the gain error at each antenna, assuming that the gain fluctuations are statistically independent. Table 2 shows the phase correction noise floor in degrees as a function of gain stability.

The gain stability requirement is very stringent. The SMA receiving systems were not designed to reach this level of stability. Specifically, the physical temperature fluctuations at the heterodyne mixing element cause variations in the conversion gain of the mixer (Battat 2005; Kooi et al. 2000; Baryshev et al. 2003). This introduces a periodic variability in the IF power that is correlated with the physical temperature of the mixer. At the SMA, the cryocooler temperature instabilities at the 4K stage are typically 40 mK ($\approx 1\%$) which limits the overall receiver gain stability to 0.5%. Therefore we designed a system to monitor the physical temperature of the mixer and adjust the gain of the IF amplification to compensate for mixer conversion gain fluctuations. This system is detailed in Section 3.

2.3. Which Observing Frequency Should be Used?

The SMA supports dual frequency operation. If one is observing in a high frequency band (e.g. 690 GHz), one may use a low frequency receiver (e.g. 230 or 345 GHz) for phase correction. It is therefore important to understand the relative phase correction performance in each of these three bands. The relevant parameters that have frequency dependence are the receiver temperature (increasing with frequency), the sky brightness temperature (generally increasing with temperature) and thus the system temperature. In addition, the atmospheric sensitivity is a strong function of frequency. Finally, as shown in Equation 3, the phase errors scale linearly with frequency for a given amount of water vapor. Thus, we evaluate Equation 18 as a function of frequency and atmospheric *pwv* content. The results are shown in Figure 9. Our conclusion is that of the three bands evaluated, the SNR per degree of phase is largest in the 230 GHz band in all but the best observing conditions. We performed our 2004 January phase correction experiments at 230 GHz.

3. Receiver Gain Stabilization System

A gain stabilization servo loop has been developed to monitor the physical temperature of the mixer and adjust the IF gain to compensate for conversion gain fluctuations in the mixer. Our

Facility	Technique	Freq (GHz)	Residual Phase (μm)
VLA	Hybrid	21, 31	2500
IRAM-PdBI	WLM	22	175
OVRO	WLM	22	160
SMA	WLM	183	150
CSO-JCMT	WLM	183	80
IRAM-PdBI	TP	90, 230	210
BIMA	TP	90	170
SMA	TP	230	90

Table 1: A summary of the current state of atmospheric phase correction. The residual phase quantifies the performance of the phase correction technique and is presented in units of μm for comparison across frequency. For reference, at 230, 345 and 690 GHz, residual electrical paths of 210, 140 and 70 μm cause 1 radian of phase error. And 36, 24 and 12 μm cause 10° of phase error. Note the same instruments were used for the CSO-JCMT and the SMA-WLM experiments, and thus the residual phases are expected to be the same, however instrumental problems degraded the quality of the phase correction. Also, during our phase correction experiment, the receiver gain stability was approximately 1 part in 1,500. With our gain stabilization system, we expect at least a factor of two improvement in the gain stability and a reduction in the residual phase.

	1 mm *pwv*			2 mm *pwv*		
$\Delta G/G$	$\Delta\phi_{230}$	$\Delta\phi_{340}$	$\Delta\phi_{680}$	$\Delta\phi_{230}$	$\Delta\phi_{340}$	$\Delta\phi_{680}$
10^{-5}	0.1	0.1	0.4	0.1	0.2	1.5
10^{-4}	1.2	1.1	4.1	1.4	1.6	15
5 x 10^{-4}	5.9	5.4	21	6.8	7.8	74
10^{-3}	12	11	41	14	16	150
5 x 10^{-3}	59	54	210	68	78	740
10^{-2}	120	110	410	140	160	1500

Table 2: The noise floor to total power phase correction as a function of the fractional gain stability of the receivers. The phase errors are listed in degrees, and depend linearly on the fractional gain stability, as described in Equation 21. The phase error also depends on the mean amount of pwv which affects both the system temperature and the atmospheric sensitivity, and we present the results for 1 and 2 mm of pwv.

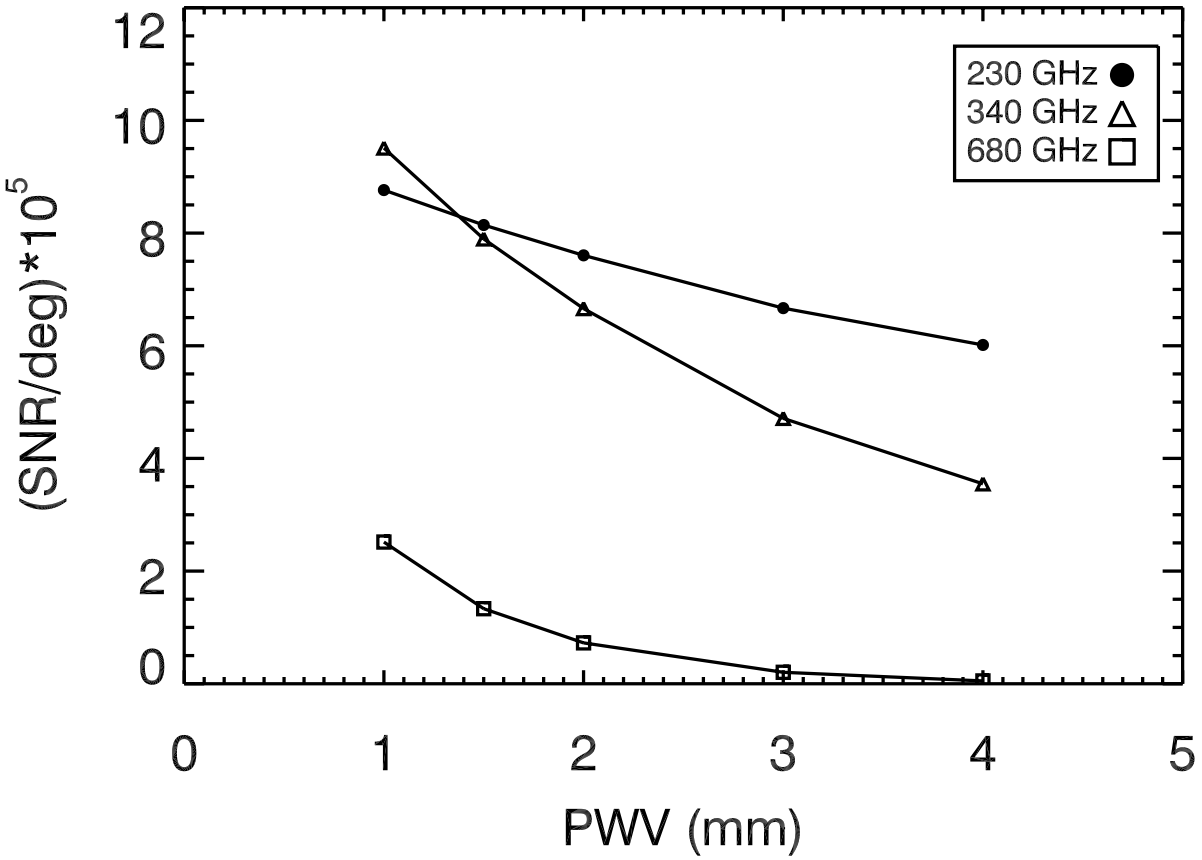

Fig. 9.— The signal to noise ratio per degree of phase error (multiplied by a factor of 10^5) as a function of *pwv* for three frequencies of interest. In all but the best weather conditions, the SNR/deg is optimal at 230 GHz. Never is the SNR/deg greatest in the 680 GHz band. This is mostly due to the large system temperatures at 680 GHz (with contributions from the atmosphere and the receiver noise). As the *pwv* drops below 1.5 mm, 340 GHz becomes the optimal frequency for phase correction. During our tests, the observing conditions were typically ∼2.5-4 mm zenith *pwv*, and so we used the 230 GHz receivers. Note that the effects of gain fluctuations were not included in this analysis, but one expects that the 230 GHz receivers are at least as stable as the other bands, and so the result that the best SNR/deg occurs at 230 GHz should continue to hold. The receiver temperatures used during this analysis were T_{rx} = 80, 120, 500 at 230, 340 and 680 GHz, respectively.

system has been successfully tested in the Submillimeter Receiver Laboratory and on three of the SMA telescopes, and is capable of stabilizing the 230 GHz receivers to 1 part in 6,000 in the lab and 1 part in 4,000 in the field (over ten minutes). This system was not in use during the 2004 January observations described below, but when implemented it would significantly improve the quality of the phase correction. See Battat (2005) for further detail of the stabilization system.

4. Phase Correction Results

Battat et al. (2004) provides a detailed analysis of a particular phase correction measurement (20 minutes on 3C 273 at 230 GHz). In this section, we present the compiled results of the SMA atmospheric phase correction experiment undertaken during 2004 January. Some relevant observing parameters are listed in Table 3.

During our experiment we measured the total power received at each antenna, P_1 and P_2. We also measured the phase of the astronomical signal, ϕ_{SMA}, using the SMA correlator. Because we did not have a reliable temperature scale for the data, we scaled the total power data into a phase prediction, ϕ_{TP} of the following form

$$\phi_{TP} = A * P_1 - B * P_2 + C. \tag{22}$$

The parameters, A, B and C were chosen to minimize the residual phase error defined by

$$\phi_{resid} \equiv \phi_{SMA} - \phi_{TP} \tag{23}$$

and were computed by minimizing the error quantity

$$\chi^2 = \sum_i \phi_{resid}^2 = \sum_i \left(\phi_{SMA} - \phi_{TP}\right)^2. \tag{24}$$

We quantify the quality of the phase correction by the standard deviation of ϕ_{resid}, keeping in mind that even in the case of perfect atmospheric phase correction, one still expects some finite rms error in ϕ_{resid} due to instrumental phase errors.

Table 4 shows the phase correction results for all usable data sets, and Figure 10 shows a histogram of the rms phase errors pre- and post-correction for the group of observations. During this experiment, the atmospheric phase stability was generally good to begin with. It was not unusual to see uncorrected rms phase errors of $20 - 30°$ at 230 GHz. Because our instrumental noise floor is roughly 20°, the improvements on the phase error were often marginal. However, when the atmospheric phase errors grew to 60, 80 or 100°, our phase correction system significantly

Nights	4 (2004 January 20, 28, 29, 30)
Hours	∼6 hours usable data
Sources	3C 273, Venus, Mars, Ganymede, Saturn
Baseline	140 m (N-S, ant 3/5, pad 12/16)
Frequency	230.5 GHz

Table 3: Some relevant details of the observing setup for the phase correction experiment at the SMA on Mauna Kea.

improved the phase errors and increased the recoverable flux by factors of 1.5-2.0. We notice that A, B and C vary with time. These parameters will depend on atmospheric properties (vertical profile of water vapor) as well as antenna properties (e.g. ground pickup). There are not enough systematic measurements to make a statement about the general behaviour of the parameters (i.e. how often and by how much they change). We can say that a parameter set generally gave good phase correction performance over a period of 20-30 minutes.

In Figures 11, 13 and 14, we show one observation during which the phase stability was poor and the phase correction was remarkably successful, one in which the phase stability was poor but the rms of the residual phase was rather large and one in which the atmospheric phase stability was good to begin with. These plots are provided to give a sense of how the phase correction behaves under various conditions. The details of the observations are provided in the figure captions and in Table 4.

5. Conclusions

We have demonstrated that total power phase correction can provide an accurate measure of the atmospheric phase error between antenna pairs and reduce the effect of atmospheric phase errors on astronomical observations. Our system is the most sensitive total power system, as quantified by the residual electrical path, that we know of. During our 2004 January phase correction experiment, our system reduced the phase errors during every observation. During several instances, the resulting coherence was improved by 50-100%. This increase in recoverable flux translates into better signal to noise for observers, or, alternatively, reduces the required observing time to achieve a particular signal to noise ratio. In addition it can enable observations in otherwise unworkable conditions.

Certainly more exploration of this technique is warranted. For example, integrating the gain stabilization into the phase correction system would further improve the quality of phase correction. In addition, it is important to carry out more detailed observations in both a range of observing conditions and over a range of azimuth and elevation to understand the timescales over which the A, B and C parameters vary. This will define how often the total power phase correction system needs calibration. Based on our experiments, I expect this timescale to be $\approx 20-40$ minutes depending on observing conditions. Alternatively, if a second calibration load (other than the ambient load) was installed in the antennas, then each receiver would have an independent temperature scale and the number of fit parameters could be reduced to one: k_ν, the scaling between brightness temperature difference and phase difference (see Equation 16).

To fully exploit the power of the SMA (high resolution imaging at high frequencies), some form of reliable atmospheric phase correction system must be developed. Different phase correction techniques have undergone extensive development at other interferometers, especially at ALMA. As yet, no consistently accurate system exists. Our data show that total power radiometry may be a viable option, worthy of further development.

6. Acknowledgements

This technical memorandum is a product of research carried out in partial fulfillment of the PhD requirements of the Harvard University Department of Astronomy. A shorter version of this

Date	Source	UT Time	Uncorrected Phase (deg)	Corrected Phase (deg)	Uncorrected Phase (μm)	Corrected Phase (μm)	Visibility Ratio	Duration (min)	τ_{225} (zenith)	PWV LOS (mm)	Comments
2004Jan30	Ganymede	13:58	29	27	105	98	1.0	6	0.15	3.7	
		14:23	22	21	80	76	1.0	10	0.14	3.6	
		14:53	30	23	108	83	1.1	22	0.14	3.9	
		15:20	32	20	116	72	1.1	9	0.13	3.8	
	3C 273	16:07	65	43	235	155	1.4	15	0.14	3.9	
		16:23	51	18	184	65	1.4	15	0.13	3.8	
		16:41	82	25	296	90	2.5	14	0.14	4.4	See Fig. 11
2004Jan29	Saturn	05:34	26	20	94	72	1.0	21	0.14	4.1	
		05:57	82	49	296	177	1.9	20	0.16	4.4	
2004Jan28	Venus	02:07	100	75	362	271	1.9	18	0.25	7.1	See Fig. 13
	Mars	04:30	25	19	90	69	1.0	22	0.20	5.0	
		04:55	27	18	98	65	1.1	25	0.20	5.2	
		05:36	27	20	98	72	1.1	14	0.20	5.7	
		05:52	20	18	72	65	1.0	6	0.20	5.9	
		06:02	25	15	90	54	1.1	11	0.21	6.4	See Fig. 14
		06:13	20	18	72	65	1.0	10	0.20	6.3	
2004Jan20	Venus	02:16	24	14	87	51	1.1	5	N/A	N/A	
		02:22	27	22	98	80	1.0	28	N/A	N/A	
		02:50	75	33	271	119	2.0	26	N/A	N/A	
		03:17	20	13	72	47	1.0	27	0.12	4.1	
		03:45	29	21	105	76	1.1	23	0.12	4.5	
		04:11	17	11	61	40	1.0	26	0.12	5.2	

Table 4: All usable data sets obtained during the 2004 January campaign of the SMA phase correction experiment. The columns show, in order, the date, source and UT time of the observation, the rms phase error before and after total power phase correction (in degrees and microns of excess electrical path), the ratio of the recoverable visibility flux with and without phase correction (1.0 = no improvement with phase correction), the duration of the observation and the observing conditions including the zenith 225 GHz opacity as measured by the JCMT and the amount of *pwv* along the line of sight, which is computed from $pwv = 25(\tau_{225} - 0.01)/\sin(\theta_{EL})$. There were no corresponding opacity measurements for three of the data sets. Three of these observations are shown in later figures.

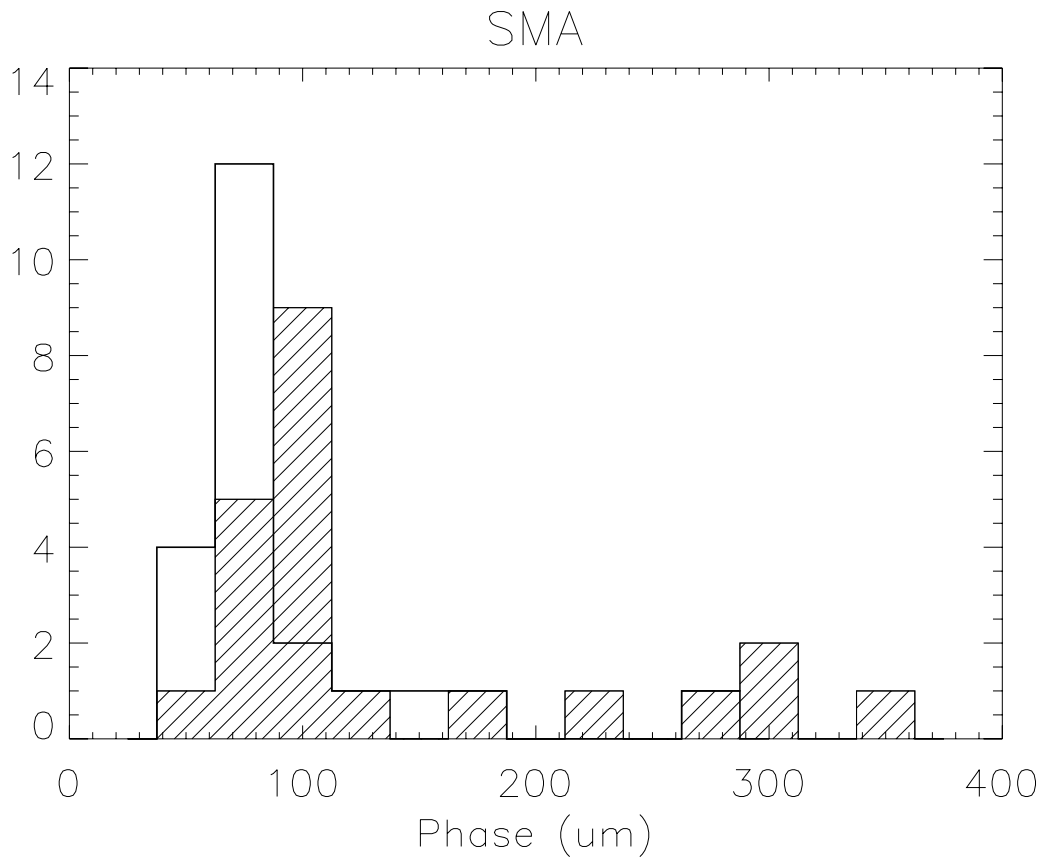

Fig. 10.— Histogram of the SMA TP phase correction experiment results for all 6 hours of observations. The shaded histogram shows the pre-correction rms phase errors, measured in μm. The unshaded histogram with a thick outline shows the post-correction rms phase errors, also in μm. The total power phase correction improves the mean of the phase data from 140 to 90 μm (from 40 to 25° at 230 GHz). The histogram bin size is 25 μm. The data from the outlying observation, ($\sim 270\mu m$ residual phase error), is shown in Figure 13.

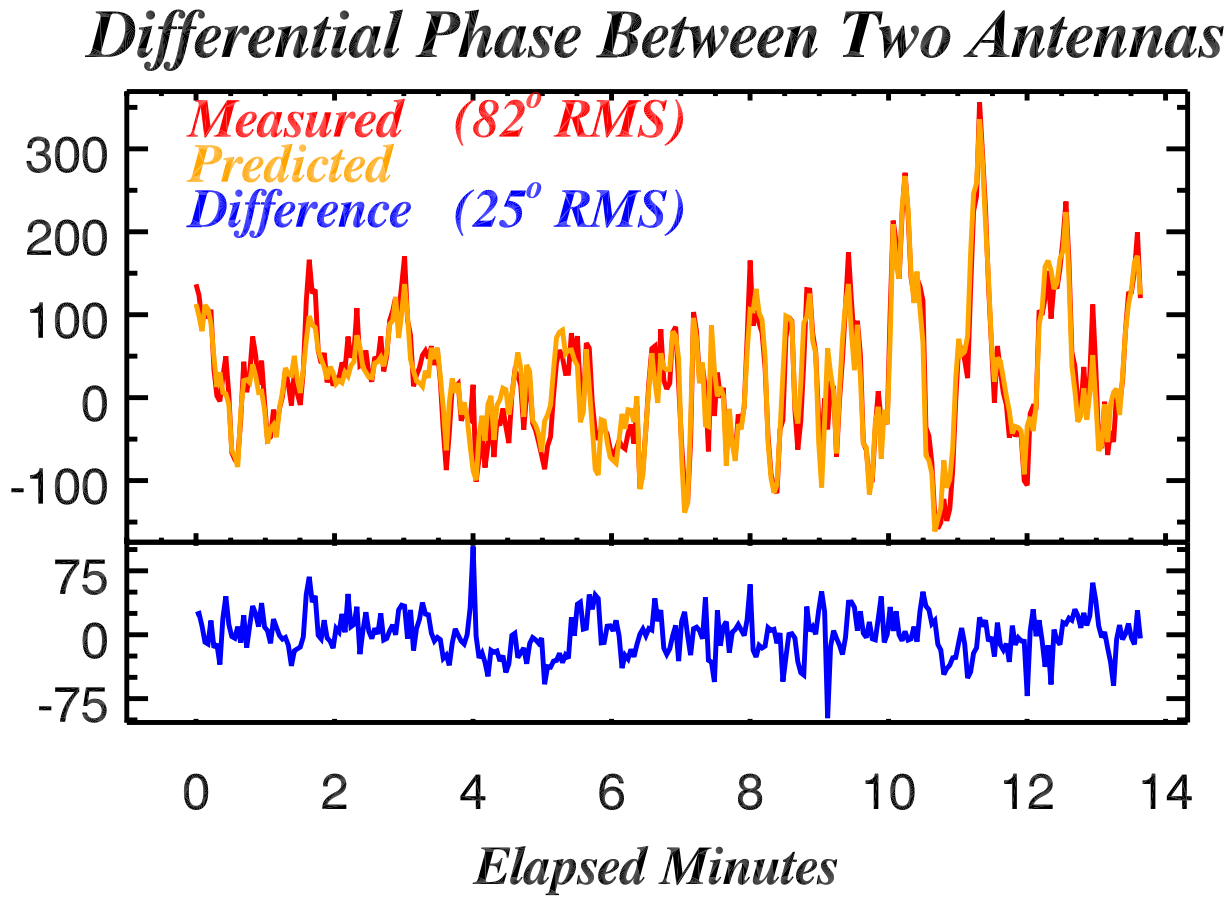

Fig. 11.— Phase correction data on 3C 273 at 230 GHz. The correlator integration time was 2.5 seconds, the 225 GHz zenith opacity was measured as 0.14 by the JCMT and the line of sight *pwv* was 4.4 mm. The phase correction does very well and improved the coherence by a factor of 2.5. The onset of the large phase fluctuations at 8 minutes was accompanied by a rapid increase in the 225 GHz opacity (from 0.14 to 0.18), see Figure 12. In this observation, the SMA phase was unwrapped with the use of the total power data. More details on this observation can be found in Battat et al. (2004).

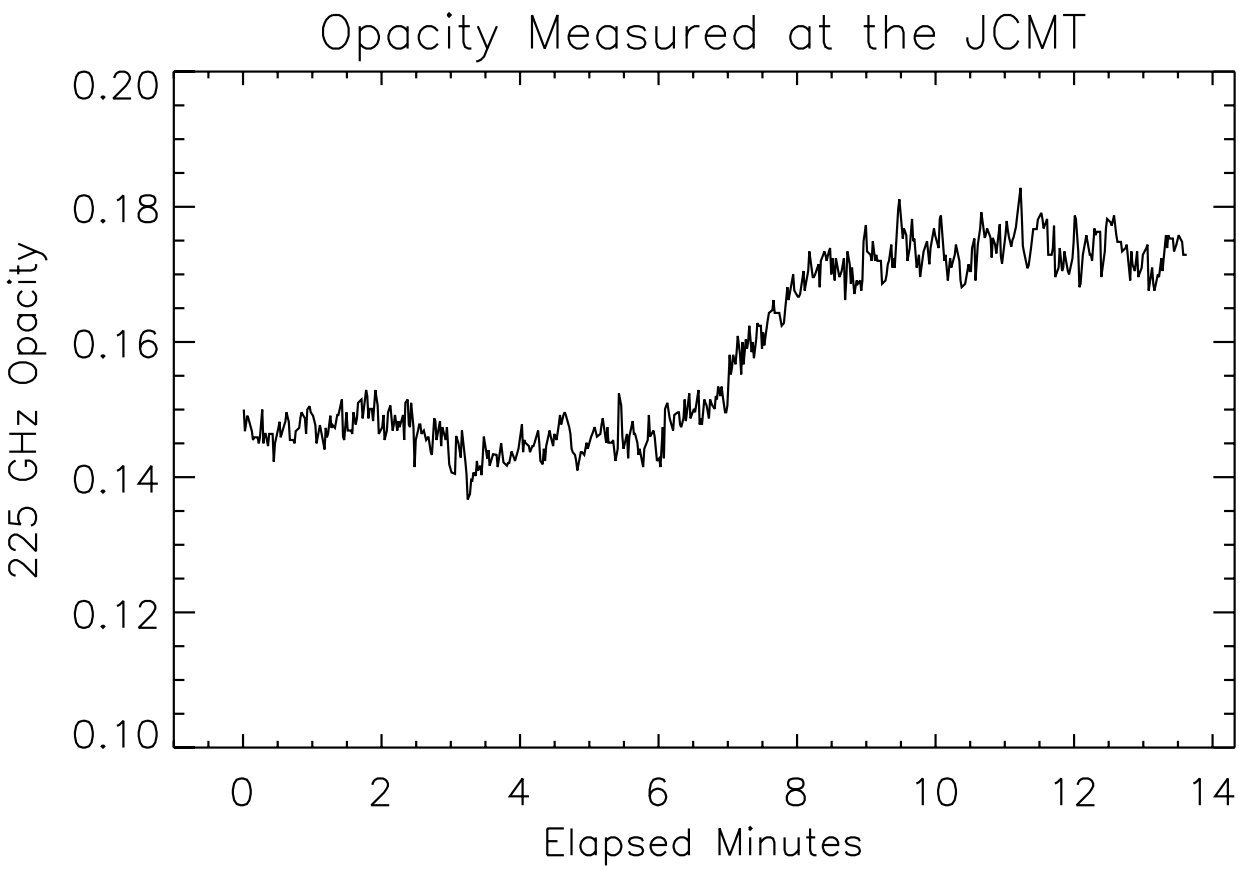

Fig. 12.— The opacity measured by the JCMT during the observation shown in Figure 11. The fast rise in opacity between minutes 6 and 8 is correlated with a rapid decay of the atmospheric phase stability.

.

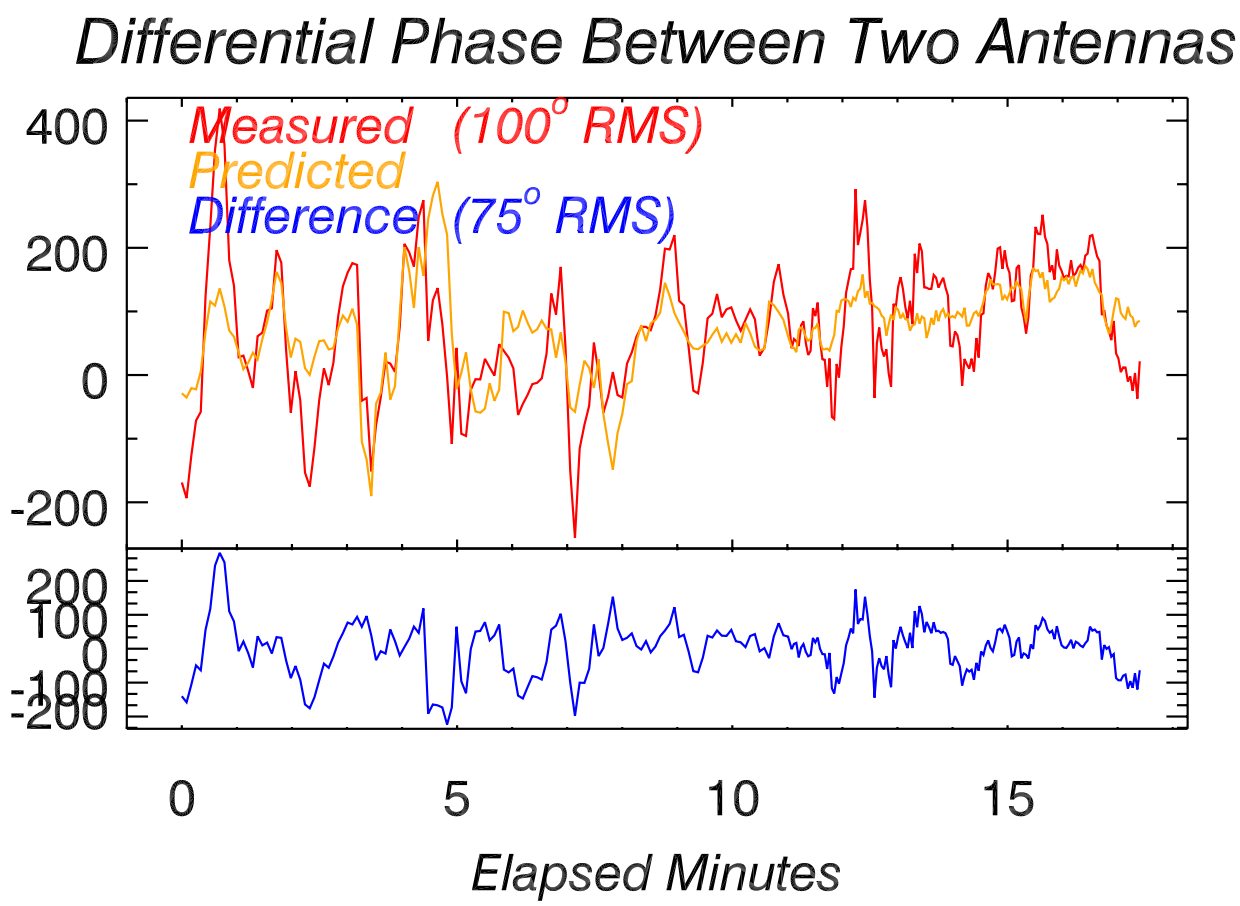

Fig. 13.— An observation of Venus at 230 GHz. The integration time was 5 seconds during the first half of the observation and 2.5 seconds in the last half. The 225 GHz opacity was 0.25, corresponding to 7.1 mm of *pwv* along the line of sight. The rms SMA correlated phase was 100° and the residual phase rms is 75°. The interferometer beam size ($\theta_{inf} \sim \lambda/b$) was 2″. During this observation, the disk size of Venus was $\sim 15''$, much larger than the interferometric beam size and a poor choice for phase calibration. Several of the phase features seen in the interferometer data have counterparts in the total power phase prediction, yet it is unclear how much of the residual phase was due to source structure and how much was due to atmospheric phase errors. Because of the high water vapor content along the line of sight, one does expect a degradation in the phase correction performance because the sensitivity parameter, $dT_{bri}/dpwv$, is small. It is unlikely that in these conditions high frequency observations ($\nu \geq 690$ GHz) would be attempted.

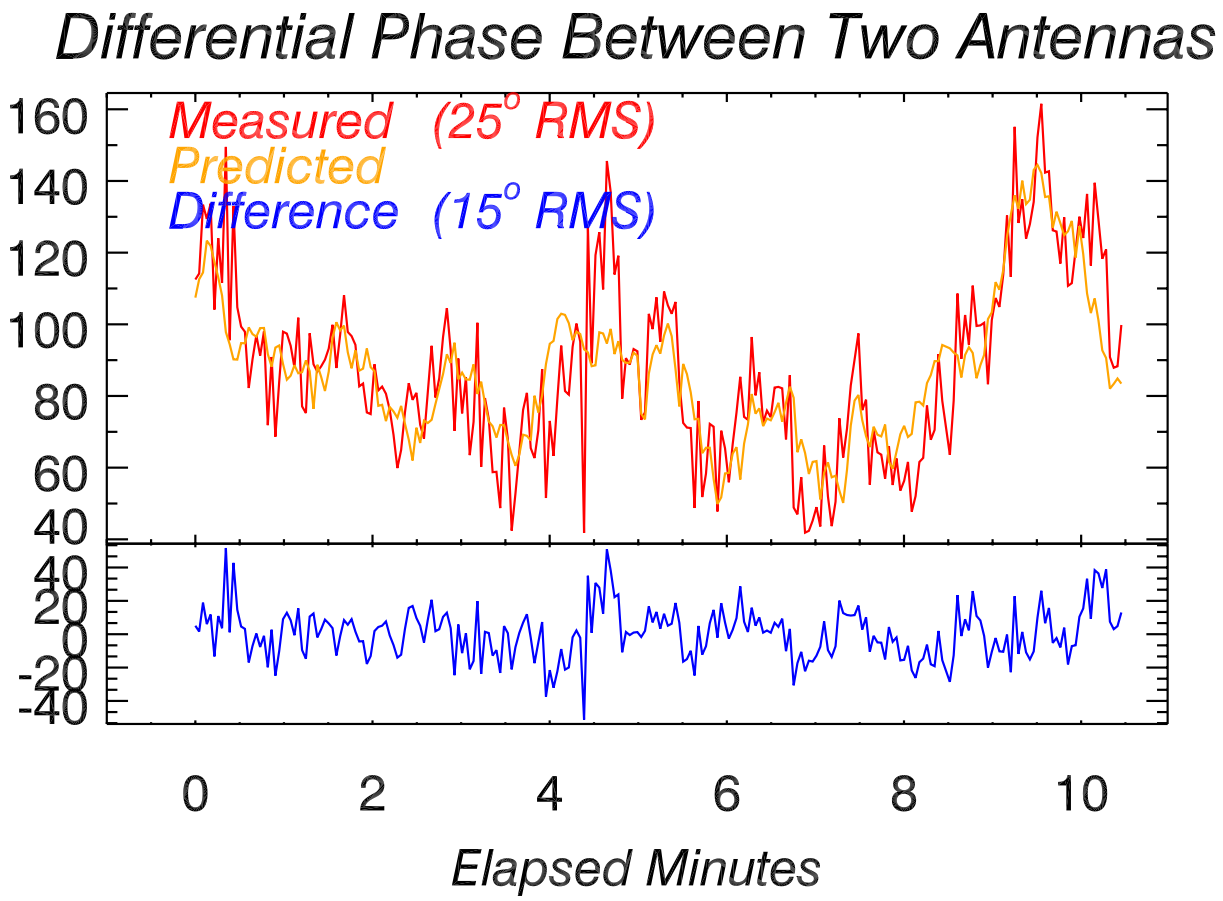

Fig. 14.— A ten minute observation of Mars at 230 GHz. The integration time was 2.5 seconds. The 225 GHz opacity was 0.21, corresponding to 6.4 mm of *pwv* along the line of sight. The atmospheric phase stability was rather good (the raw rms phase is 25°) and, to first order, the total power system tracked the phase fluctuations. However, a strong feature around 4.5 minutes was missed by the total power system, and the most rapid fluctuations were not tracked precisely. The rms of the residual phase is 15° at 230 GHz, or 55 μm of differential excess electrical path.

memorandum detailing a particular 20 minute phase correction observation was published in the Astrophysical Journal Letters special issue devoted to the SMA (Battat et al. 2004). A paper detailing the novel receiver gain stabilization system has been accepted for publication in IEEE Transactions on Microwave Theory and Techniques.

As is the case with all collaborative projects, this work owes its success to innumerable people. Several members of this group, however, have made invaluable contributions and they deserve special mention. I would like to extend my appreciation to my advisors, James Moran and Raymond Blundell for steadfast support right the way through, and for the wonderful opportunities they have provided. Martina Wiedner has shared with me her extensive understanding of and experience with atmospheric phase correction at submillimeter wavelengths. The support of the Submillimeter Receiver Lab team has been fantastic in all aspects from design to fabrication, assembly and installation. Each member has made specific, tangible contributions to this work. In addition, the site crew at the SMA, especially Rob Christensen, was instrumental in the success of the observations themselves. One more special thank you is due to Robert Kimberk for his persistent motivation and for exposing me to his unique approach to science and thought.

REFERENCES

Baryshev, A., Hesper, R., Gerlofsma, G., Kroug, M., & Wild, W. 2003, unpublished

Battat, J. B. 2005, IEEE TMTT, in press

Battat, J. B., Blundell, R., Moran, J. M., & Paine, S. 2004, ApJ, 616, L71

Butler, B. 2003, ALMA Memo Series #478

Carilli, C. L. & Holdaway, M. A. 1999, Radio Science, 34, 817

Desai, K. 1993, PhD thesis, University of California at Santa Barbara

Ho, P. T. P., Moran, J. M., & Lo, K. Y. 2004, ApJ, 616, L1

Kooi, J. W., Chattopadhyay, G., Thielman, M., & Phillips, T. G. 2000, Int. J. IR and MM Waves, 21, 689

Masson, C. R. 1994, in ASP Conf. Ser. 59: IAU Colloq. 140: Astronomy with Millimeter and Submillimeter Wave Interferometry, 87

Matsushita, S. & Matsuo, H. 2003, PASJ, 55, 325

Paine, S., Blundell, R., Papa, D. C., Barrett, J. W., & Radford, S. J. E. 2000, PASP, 112, 108

Paine, S. 2004, SMA Technical Memo #152

Peterson, J. B., Radford, S. J. E., Ade, P. A. R., Chamberlin, R. A., O'Kelly, M. J., Peterson, K. M., & Schartman, E. 2003, PASP, 115, 383

Robson, Y., Hills, R., Richer, J., Delgado, G., Nyman, L., Otárola, A., & Radford, S. 2001, ALMA Memo Series #345

Sutton, E. C. & Hueckstaedt, R. M. 1996, A&AS, 119, 559

Thompson, A. R., Moran, J. M., & Swenson, G. W. J. 2001, Interferometry and Synthesis in Radio Astronomy, 2nd edn. (New York: Wiley)

Tiuri, M. E. & Räisänen, A. V. 1986, in Radio Astronomy (Powell, OH: Cygnus-Quasar Books), John D. Kraus is the author of the book but not this chapter

Tong, C.-Y. E. 2004, personal communication

Woody, D., Carpenter, J., & Scoville, N. 2000, in ASP Conf. Ser. 217: Imaging at Radio through Submillimeter Wavelengths, 317